

Demographics of Wandering Black Holes Powering Off-Nuclear Tidal Disruption Events

MURYEL GUOLO  ¹¹ Bloomberg Center for Physics and Astronomy, Johns Hopkins University, 3400 N. Charles St., Baltimore, MD 21218, USA

ABSTRACT

The recent discovery of three off-nuclear tidal disruption events (EP240222a, AT2024tvd, and AT2025abcr)—following the first such source, 3XMM J2150–05—reveals a small but robust population of off-nuclear, or “wandering,” black holes (WBHs) with masses $M_\bullet > 10^4 M_\odot$. Two demographic trends are already apparent: (i) all events occur in massive, early-type parent galaxies with stellar masses $10.8 \lesssim \log_{10}(M_\star/M_\odot) \lesssim 11.1$; and (ii) events at larger halo-centric radii (R_{TDE}/R_{200}) are associated with dwarf satellites ($M_\star \sim 10^7 M_\odot$), while those closer to halo centers lack detected stellar counterparts. Using results from the ROMULUS cosmological simulation, we show that both trends naturally arise from hierarchical galaxy formation. By combining the simulation with empirical constraints on the local galaxy population, we compute the volumetric density of WBHs, $\phi_{\text{WBH}}(M_\star)$, finding that it peaks at $\log_{10}(M_\star/M_\odot) = 11.10^{+0.05}_{-0.10}$ and that more than half of all WBHs in the local Universe reside in galaxies with $10.7 \lesssim \log_{10}(M_\star/M_\odot) \lesssim 11.2$, explaining (i) and predicting its persistence as the sample grows. We further show that ii), i.e., the observed link between detection of stellar counterparts and R_{TDE}/R_{200} , is also expected from tidal stripping. These results demonstrate that off-nuclear TDEs are powered by the population of WBHs long predicted by cosmological simulations.

Keywords: Intermediate-mass black hole (816) Supermassive black holes (1663); Elliptical galaxies (456); Ultracompact dwarf galaxies (1734) ;

1. INTRODUCTION

It is now established that nearly all massive galaxies host a massive black hole (MBH) at their centers (Kormendy & Ho 2013). MBH masses correlate strongly with the properties of their host galaxies’ central regions (Magorrian et al. 1998; Ferrarese & Merritt 2000; Tremaine et al. 2002; Gültekin et al. 2009), indicating a co-evolution of black holes and galaxies over cosmic time (e.g., Volonteri et al. 2003; Natarajan 2014).

In the standard paradigm of galaxy formation, MBHs grow primarily through gas accretion in galactic nuclei, producing active galactic nuclei (AGN), while galaxies assemble hierarchically through mergers. This process naturally leads to a population of MBHs¹ that are displaced from galaxy centers in the local Universe.

The pathway from galactic scales to the coalescence of MBH binaries in galactic centers involve multiple physical processes operating across wide spatial and tem-

poral scales (Begelman et al. 1980; Colpi 2014). Only MBHs that efficiently sink to galactic centers can form bound binaries and eventually merge, producing gravitational waves detectable by space-based interferometers such as LISA (Amaro-Seoane et al. 2017). In many systems, however, orbital decay stalls at kiloparsec scales, where dynamical friction dominates (Chandrasekhar 1943) and can exceed a Hubble time for sufficiently low-mass MBHs. As a result, a substantial population of off-nuclear MBHs is expected to persist to low redshift.

The existence of these long-lived, off-nuclear massive black holes was predicted based on semi-analytical calculations, well before modern hydrodynamical simulations, as a natural consequence of hierarchical galaxy assembly and inefficient orbital decay (e.g., Governato et al. 1994; Volonteri et al. 2003; Islam et al. 2004; Bellovary et al. 2010).

Nowadays cosmological simulations are the primary theoretical tool for studying this population of wandering black holes (WBHs), here defined as MBHs not located at the center of their main galactic halo or residing in satellite substructures. In particular, those simulations that seed black holes based on local gas properties,

¹ Here MBHs are defined as black holes not formed through standard stellar evolution, i.e., with masses $M_\bullet \gg 10^3 M_\odot$, including intermediate-mass black holes (IMBHs; $10^3 \ll M_\bullet \lesssim 10^5 M_\odot$) and supermassive black holes (SMBHs; $M_\bullet \gg 10^5 M_\odot$).

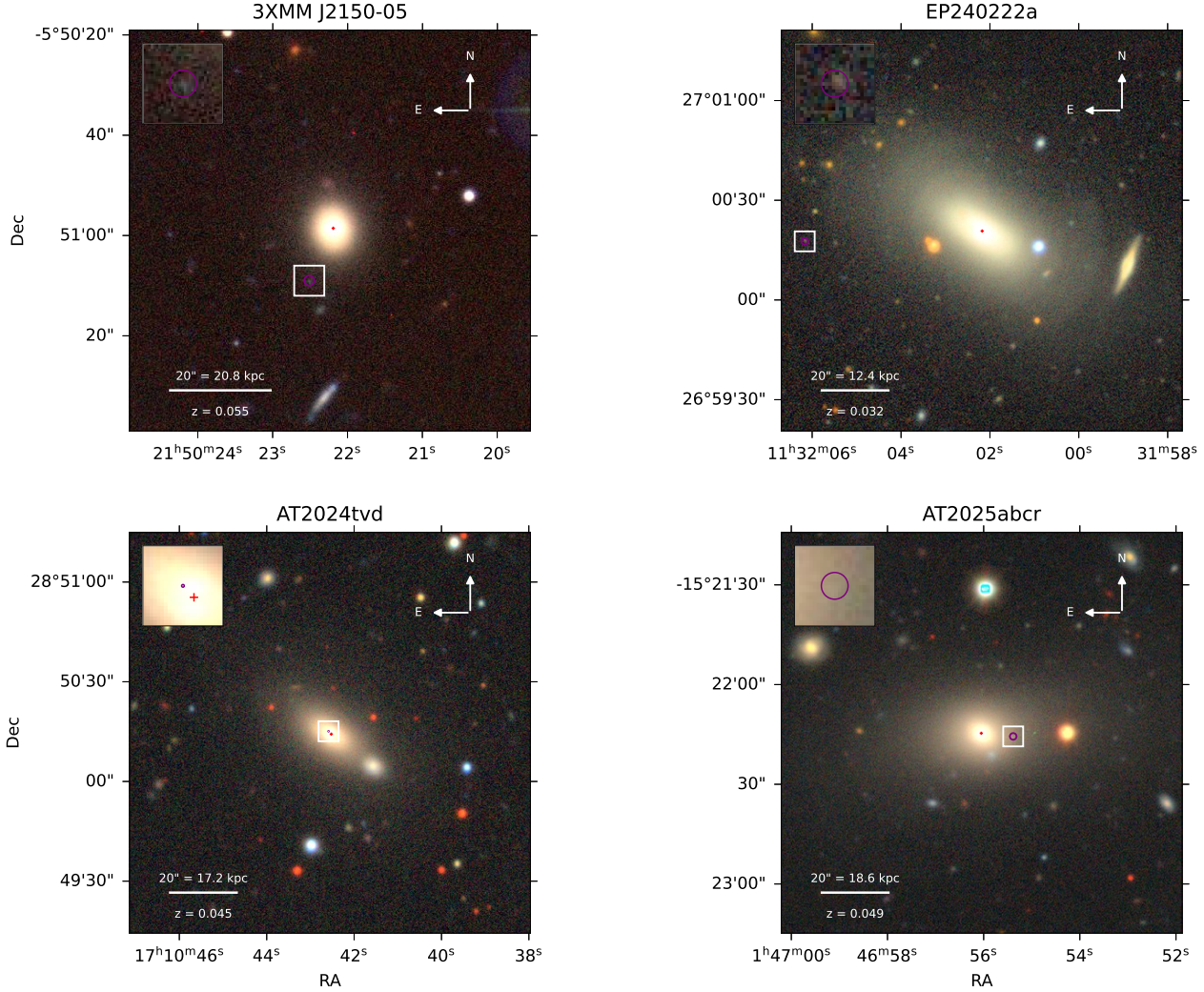


Figure 1. Pre-TDE optical imaging of the parent galaxies of the four known off-nuclear tidal disruption events. For each source, the panel shows a color composite of the host galaxy and a zoomed-in view centered on the TDE location. Purple circles mark the most precise positions of the transients, derived from space-based X-ray or ultraviolet observations. Pronounced stellar overdensities consistent with bound dwarf satellites are detected for 3XMM J2150–05 and EP240222a, whereas no resolved stellar counterpart is visible at the locations of AT2024tvd and AT2025abcr above the smooth halo light. The stellar counterpart overdensities (or lack thereof) are quantified in Appendix C, and the results are shown in Table 1.

incorporate subgrid prescriptions for dynamical friction, and allow MBHs to orbit freely rather than being artificially repositioned at halo centers. Notable examples include ROMULUS (Tremmel et al. 2017) and ASTRID (Ni et al. 2022) simulations.

Studies based on ROMULUS find a roughly linear scaling between the number of WBHs per halo and the halo virial mass, with Milky Way-like halos hosting order ten WBHs (Tremmel et al. 2018a) and massive galaxy clusters hosting more than a thousand (Ricarte et al. 2021b). Despite their predicted abundance, WBHs are expected to accrete weakly in the local Universe, with typical Eddington ratios $\lesssim 10^{-4}$ (Ricarte et al. 2021a), owing to gas-poor environments and the lack of efficient angular-

momentum diffusion mechanisms, such as those available to secularly fed central SMBHs (Storchi-Bergmann & Schnorr-Müller 2019). This makes them extremely difficult to detect directly, and observationally WBHs have therefore proven elusive.

Non-accreting WBHs have been inferred dynamically in a small number of ultra-compact dwarf galaxies (UCDs; e.g., Seth et al. 2014; Taylor et al. 2025), which are common in galaxy clusters (Pfeffer et al. 2014; Voggel et al. 2019). Accreting WBHs have been proposed to appear as off-nuclear AGN, particularly in merging systems (Comerford et al. 2009; Comerford & Greene 2014; Reines et al. 2020; Ward et al. 2021; Upal et al. 2024), but such sources are rare and often

ambiguous (e.g., [Sturm et al. 2026](#)), being difficult to distinguish from recoiling SMBHs or from dual, similar-mass AGN produced by major mergers. WBHs (of intermediate mass) have also been invoked as engines of some ultra-luminous X-ray sources (ULXs; $L_X \gtrsim 10^{39} \text{ erg s}^{-1}$), although most objects in this class are now understood to be extreme stellar-mass accretors ([Kaaret et al. 2017](#)). A notable exception is ESO 243-49 HLX-1 ([Farrell et al. 2009](#); [Soria et al. 2017](#)), which reaches $L_X \sim 10^{42} \text{ erg s}^{-1}$ and provided the first strong case for an accreting off-nuclear IMBH; however, this source appears unique, and the physical origin of its repeating outbursts remains unclear.

If the WBHs retain some bound stellar population, tidal disruption events (TDEs, [Rees 1988](#); [Gezari et al. 2021](#)) can supply the accreting material needed to briefly power luminous emission. Such off-nuclear TDEs therefore provide one of the most direct and unambiguous probes of WBHs. Unlike AGN, black hole masses in TDEs can be inferred directly from multi-wavelength modeling based on first principle models, independent of any scaling relations (like those based on single-epoch broad line emission measurements, which are poorly calibrated at the low mass end of interest here) enabling, e.g., black hole–host scaling relations to be recover independently (e.g., [Mummery et al. 2024](#); [Guolo et al. 2025](#)).

The discovery of 3XMM J215-05 in 2018 ([Lin et al. 2018, 2020](#)) marked the first off-nuclear TDE. Over the past year, three additional sources have been identified: EP240222a ([Jin et al. 2025](#)) by *Einstein Probe* ([Yuan et al. 2018](#)), and AT2024tvd ([Yao et al. 2025](#)) and AT2025abcr ([Stein et al. 2026](#)) by the Zwicky Transient Facility ([Bellm et al. 2019](#)).

Despite the small current sample, two demographic trends are already apparent. All events occur in massive, early-type parent galaxies with total stellar masses in the order of $M_\star \sim 10^{11} M_\odot$. In addition, the two events at larger halo-centric radii (R_{TDE}/R_{200}) are associated with dwarf satellite galaxies ($M_\star \sim 10^7 M_\odot$), while those occurring closer to halo centers lack detectable stellar counterparts. The goal of this *Letter* is to show that these trends arise naturally from hierarchical galaxy and black hole assembly and can be extracted from the **ROMULUS** simulation results. In §2 we describe the off-nuclear TDE sample and simulation data; in §3 we present our results; and we conclude in §4. In this paper we adopt a flat λCDM cosmology, with $H_0 = 69 \text{ km s}^{-1} \text{ Mpc}^{-1}$ ([Planck Collaboration et al. 2020](#)); uncer-

tainties (error-bars and contours) are reported as 68% credible intervals, unless otherwise stated.

2. OFF-NUCLEAR TDES AND THE ROMULUS SIMULATIONS

2.1. Sample and Properties

Our sample consists of four sources: 3XMM J215-05, EP20240222a, AT2024tvd, and AT2025abcr. These sources share several defining properties: (i) transient multi-wavelength light curves; (ii) detections spanning X-ray through UV/optical wavelengths; (iii) super-soft/thermal X-ray spectra, a unique feature of TDEs ([Guolo et al. 2024](#)); (iv) peak X-ray luminosities $L_X > 10^{42} \text{ erg s}^{-1}$ (excluding stellar-mass accretors); and (v) when early-time optical spectra are available (all except 3XMM J215-05), the presence of transient broad Balmer emission lines and, in some cases, higher-ionization features such as He II and Bowen fluorescence, similar to those observed in nuclear TDEs ([Charalampopoulos et al. 2022](#)). Crucially, however, all four sources are significantly displaced from the centers of their parent galaxies, with projected offsets ranging from $0.9''$ to $53''$. These properties are individually all characteristic of TDEs (e.g., [van Velzen et al. 2021](#); [Charalampopoulos et al. 2022](#); [Yao et al. 2023](#); [Guolo et al. 2024](#); [Mummery et al. 2024](#); [Grotova et al. 2025](#); [Mummery & van Velzen 2025](#)) and, when considered together, make these events the most secure cases of off-nuclear TDEs currently known.

Two additional sources, eRASS J1421-29 ([Grotova et al. 2025](#)) and 4XMM J1615+19 (also known as NGC 6099 HLX-1; [Chang et al. 2025](#)), are, in our view, likely to be genuine off-nuclear TDEs. However, the analyses presented for these sources and/or the currently available data are, in our view, yet insufficient to conclusively rule out alternative explanations. We therefore do not include them in our sample².

A third source, WINGS J1348+26 ([Maksym et al. 2013](#); [Donato et al. 2014](#)), is a TDE originating from the nucleus of a dwarf galaxy ($M_\star \sim 10^8 M_\odot$), spectroscopically confirmed to be associated with the galaxy cluster Abell 1795 ([Maksym et al. 2014](#)). In some sense, this event could be considered “off-nuclear” with respect to the cluster center (and its brightest cluster galaxy, BCG) and would qualify as such under the definition of wandering black holes in **ROMULUS**. At this point, however, this classification becomes largely a matter of semantics

² Importantly, both sources seem to be associated with massive early-type galaxies with stellar masses similar to those of our hosts. Including them would not alter our conclusions regarding the galaxy-mass preference discussed in §3.1.

Table 1. Host and halo properties of off-nuclear TDEs

Source	z	$R_{\text{TDE,p}}$	$\log_{10} M_{\star}$	$R_{1/2}$	$\log_{10} M_{200}$	R_{200}	R_{TDE}	R_{TDE}/R_{200}	$\Sigma_{\star,\text{local}}/\Sigma_{\star,\text{halo}}$
		(arcsec, kpc)	(M_{\odot})	(arcsec, kpc)	(M_{\odot})	(kpc)	(kpc)		
3XMM J2150-05	0.055	11.6, 12.6	10.87 ± 0.06	2.3, 2.5	$12.6^{+0.2}_{-0.3}$	$329.0^{+46.0}_{-61.0}$	$15.7^{+7.4}_{-2.9}$	$0.052^{+0.023}_{-0.014}$	3.6 ± 0.1
EP240222a	0.032	53.1, 34.4	10.98 ± 0.07	12.1, 7.8	$13.0^{+0.2}_{-0.3}$	$448.0^{+64.0}_{-88.0}$	$43.0^{+20.2}_{-8.1}$	$0.106^{+0.047}_{-0.030}$	7 ± 2
AT2024tvd	0.045	0.9, 0.8	10.84 ± 0.07	5.3, 4.8	$12.7^{+0.2}_{-0.3}$	$337.0^{+47.0}_{-64.0}$	$1.0^{+0.5}_{-0.2}$	$0.003^{+0.001}_{-0.001}$	1
AT2025abcr	0.049	9.5, 9.2	11.11 ± 0.08	8.0, 7.8	$13.3^{+0.2}_{-0.3}$	$565.0^{+82.0}_{-114.0}$	$11.5^{+5.4}_{-2.2}$	$0.023^{+0.010}_{-0.007}$	1

and arbitrary definitions, and we choose not to include this source in our sample.

We also do not include luminous fast blue optical transients (LFBOTs; e.g., [Perley et al. 2019](#); [Ho et al. 2023](#); [Somalwar et al. 2025](#)) or ESO 243-49 HLX-1. Although these sources have been interpreted as TDEs by some authors, their observed properties—including light-curve evolution, repeating of outbursts, and/or spectral characteristics—are fundamentally distinct from those of the off-nuclear TDEs analyzed here, suggesting a different physical origin.

Having selected and described our sample, Fig. 1 shows pre-TDE color images of the four parent galaxies, with zoomed-in regions indicating the TDE locations. Images are taken from the Legacy Survey ([Dey et al. 2019](#)) for all sources except 3XMM J215-05, for which deeper pre-TDE CFHT MegaCam ([Gwyn 2012](#)) data are available. The purple circles mark the most precise transient positions, derived from space-based UV or X-ray observations using either *Chandra* ($\sim 1''$ PSF) or *HST* ($\sim 0.1''$ PSF). Clear stellar overdensities are visible at the locations of 3XMM J215-05 and EP20240222a, but not for AT2024tvd or AT2025abcr. The latter is confirmed by detailed image decomposition analyses presented by [Yao et al. \(2025\)](#) and [Stein et al. \(2026\)](#).

In Table 1, we summarize the basic parent-galaxy properties: redshift (z); projected ($R_{\text{TDE,p}}$) and deprojected (R_{TDE}) offsets of the TDEs from their host nuclei; stellar (M_{\star}) and virial (M_{200}) masses; half-light ($R_{1/2}$) and virial (R_{200}) radii; and the ratio of local to halo stellar surface densities ($\Sigma_{\star,\text{local}}/\Sigma_{\star,\text{halo}}$). Projected offsets are taken from the discovery papers, while deprojected distances assume an isotropic orientation distribution, i.e., $R_{\text{TDE}} = \frac{R_{\text{TDE,p}}}{\sin(\theta)}$, with $P(\theta) \propto \cos \theta$. Half-light radii are taken from the Legacy Survey Data Release 10 ([Dey et al. 2019](#)), and virial masses and radii are inferred from M_{\star} and $R_{1/2}$ as described in Appendix A.

Rather than relying on heterogeneous (distinct stellar population models and/or apertures) stellar-mass estimates from the literature, we measure parent-galaxy stellar masses in a uniform manner. As described in

Appendix B, we adopt a color-dependent mass-to-light ratio (M_{\star}/L_i) applied to Sérsic-profile luminosities, following the same approach used by [Baldry et al. \(2012\)](#) to derive the local galaxy stellar mass function. This choice is essential for our comparison with GMSF predictions in §3. Our derived stellar masses are consistent with those reported in the discovery papers, typically within ~ 0.1 dex, but at most ~ 0.2 dex, which does not affect our conclusions. Finally, the local-to-halo stellar overdensities for 3XMM J215-05 and EP20240222a are calculated using the deepest available pre-TDE imaging—*HST* and the Legacy Survey, respectively—as described in Appendix C.

We do not present black hole mass estimates for the full sample. A reliable and uniform method capable of recovering black hole–host scaling relations has not yet been applied to all four sources. The method of [Guolo & Mummery \(2025\)](#) has been applied to AT2024tvd and 3XMM J215-05 [Guolo et al. \(2025, 2026\)](#), finding that the black hole powering AT2024tvd is approximately $\sim 10^6/10^{4.4} \simeq 40$ times more massive than that of 3XMM J215-05. Comparable estimates are unavailable for the remaining events, precluding a homogeneous comparison. Moreover, in the **ROMULUS** simulations all black holes are seeded with the same initial mass, $M_{\bullet} = 10^6 M_{\odot}$, preventing a direct comparison between simulated and observed black hole masses.

2.2. *ROMULUS* Simulation

We summarize here the aspects of massive black hole (MBH) modeling in the **ROMULUS** simulations most relevant to this work; full technical details are provided in [Tremmel et al. \(2017, 2019\)](#); [Ricarte et al. \(2021b\)](#). The simulation suite consists of **ROMULUS25**, a (25 Mpc)³ cosmological volume, and **ROMULUSC**, a higher-resolution zoom-in simulation of a galaxy cluster with $M_{200} \sim 10^{14} M_{\odot}$. Both were run using the Tree+SPH code **ChaNGa** ([Menon et al. 2015](#); [Wadsley et al. 2017](#)), with dark matter and gas particle masses of $3.4 \times 10^5 M_{\odot}$ and $2.1 \times 10^5 M_{\odot}$, respectively.

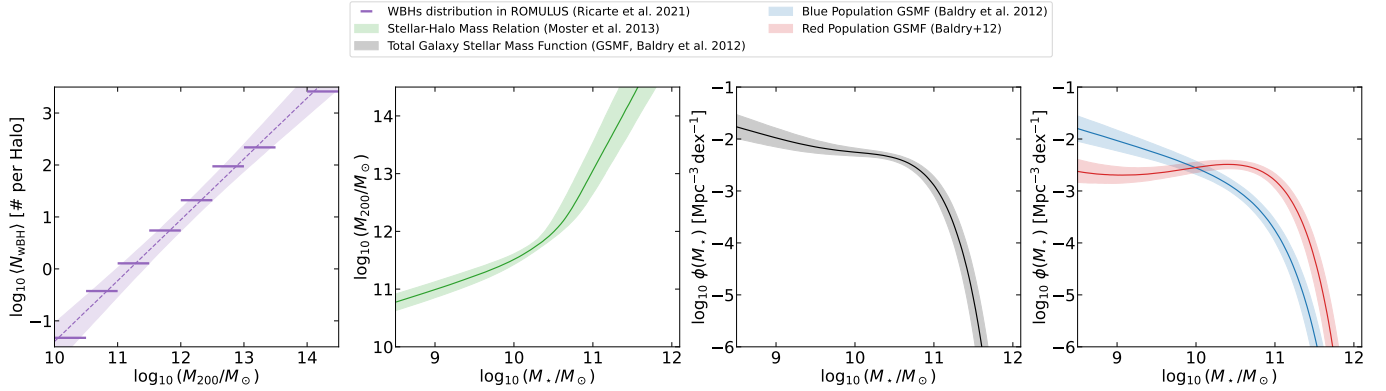


Figure 2. *Left:* Mean number of wandering black holes per halo as a function of halo virial mass at $z \simeq 0.05$ in the **ROMULUS** simulations, reproduced from Ricarte et al. (2021b). Purple points show the binned simulation results, the dashed line shows the best-fitting power-law relation, and the shaded region indicates the 1σ uncertainty. *Middle left:* Stellar-to-halo mass relation at $z \simeq 0$ from Moster et al. (2013), mapping halo virial mass to galaxy stellar mass. *Middle right:* Total galaxy stellar mass function (GMSF) in the local Universe from Baldry et al. (2012). Together, these components are combined to compute the volumetric density of wandering black holes, shown in Fig. 3. *Right:* Decomposition of the GMSF into blue (star-forming) and red (quenched) galaxy populations, also from Baldry et al. (2012).

The simulations include a correction for unresolved gravitational forces below scales of 350 pc (the so-called softening length), which would otherwise underestimate the dynamical friction acting on moving MBHs. This correction follows the classical formulation of Chandrasekhar (1943), allowing MBHs to orbit freely within their host halos rather than being artificially pinned to galaxy centers (Tremmel et al. 2015). MBH mergers are permitted once pairs become gravitationally bound within two softening lengths, corresponding to ~ 0.7 kpc. This work directly adopts the **ROMULUS** post-processing analysis presented in Ricarte et al. (2021b). In that study, halos were identified using the AMIGA halo finder (Knollmann & Knebe 2009), which was used to measure halo masses, radii, and centers. MBHs were assigned to halos or substructures based on gravitational binding, and halo centers were determined with an accuracy limited by the gravitational softening length of 350 pc.

In Ricarte et al. (2021b), MBHs were classified as “central” if located within 0.7 kpc of the halo center and as “wandering” otherwise. This definition allows for multiple central MBHs within a single halo and permits even the most massive or luminous MBH to be classified as wandering. The adopted threshold reflects uncertainties in MBH dynamics and center determination and corresponds to the scale below which MBH mergers are allowed. Beyond this radius, MBH orbits are well resolved and not artificially close to merging.

Here we explicitly use three results describing the low-redshift ($z \sim 0.05$) wandering black hole population reported by Ricarte et al. (2021b). These results are dis-

cussed in detail in the next section, but are summarized here for convenience:

- The mean number of wandering black holes per halo increases approximately linearly with halo virial mass, reflecting the cumulative impact of hierarchical mergers and satellite accretion. This is shown in the left panel of Fig. 2.
- By $z \sim 0$, most wandering black holes no longer retain a resolved stellar counterpart as a result of tidal stripping; those that do are preferentially found at larger halo-centric distances.
- Wandering black holes populate a broad range of halo-centric distances, with a characteristic concentration at intermediate radii ($0.01 \lesssim R_\bullet/R_{200} \lesssim 0.1$), and an extended distribution reaching from the halo nucleus to near the virial radius.

3. RESULTS AND DISCUSSION

3.1. Parent Galaxy Preference

From Table 1 it is immediately apparent, as first noted by Yao et al. (2025), that the parent galaxies of off-nuclear TDEs share remarkably similar global properties. All four events occur in massive, early-type galaxies, with total stellar masses confined to the narrow range $10.8 \lesssim \log_{10}(M_*/M_\odot) \lesssim 11.1$. Given the small current sample, this uniformity is striking and suggests an underlying physical or demographic origin rather than a coincidence.

This combination of high stellar mass and early-type morphology is notably *not* characteristic of the hosts of

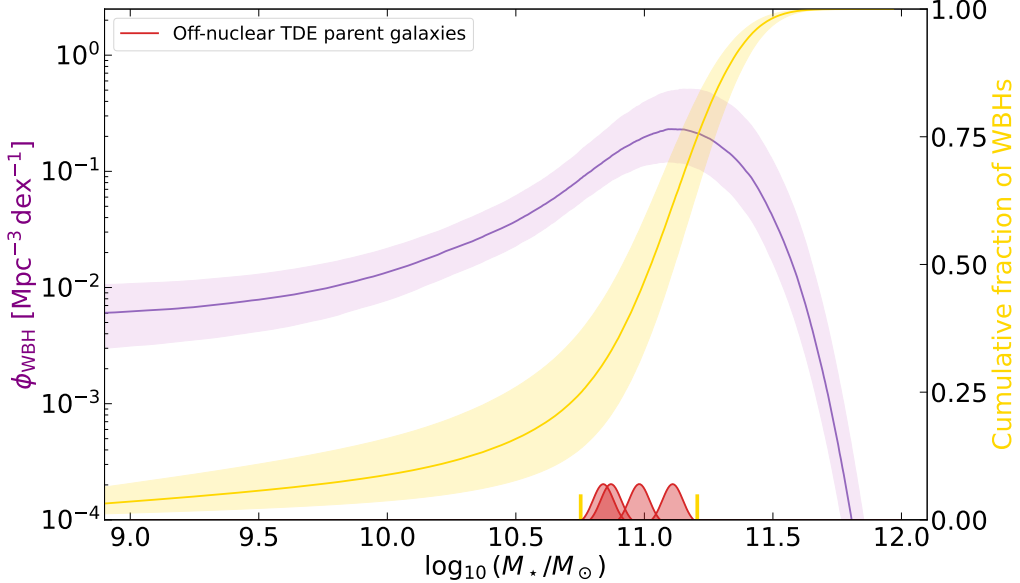


Figure 3. Volumetric density of wandering black holes as a function of parent galaxy stellar mass at $z \simeq 0$, constructed by combining the **ROMULUS** wandering black hole occupation statistics with the local galaxy stellar mass function. The purple curve shows $\phi_{\text{WBH}}(M_*)$, while the gold curve shows the cumulative fraction of wandering black holes. The distribution peaks sharply (note the log scale) at $M_* \sim 10^{11.1} M_\odot$, and half of the WBH should be located in galaxies with $10.7 \lesssim \log_{10}(M_*/M_\odot) \lesssim 11.2$ (gold ticks), explaining why all off-nuclear TDE parent galaxies (red kernels) are in this mass range.

nuclear TDEs (Hammerstein et al. 2021; Yao et al. 2023; Mummery & van Velzen 2025). Early-type galaxies in this mass regime typically have central stellar velocity dispersions $\sigma_* \gtrsim 200 \text{ km s}^{-1}$, implying central black hole masses $M_\bullet \gtrsim 10^{8.5} M_\odot$ based on the $M_\bullet - \sigma_*$ relation (Kormendy & Ho 2013). At these masses, the nuclear TDE rate is super-exponentially suppressed by the Hills mass effect (Yao et al. 2023; Mummery & van Velzen 2025), since stars are swallowed whole for most combinations of stellar mass and black hole spin. This follows from the different scaling of the tidal radius ($r_T \propto M_\bullet^{1/3}$) and the event horizon ($r_H \propto M_\bullet$) with black hole mass.

We now show that the preference for this specific class of galaxies arises naturally from the demographics of wandering black holes predicted by **ROMULUS**, once combined with the observed local galaxy population. To this end, we compute the volumetric density of wandering black holes as a function of parent galaxy stellar mass, $\phi_{\text{WBH}}(M_*)$.

As discussed in §2.2 and shown in the left top panel of Fig. 2, the mean number of WBHs per halo in **ROMULUS** scales approximately linearly with halo virial mass. The simulation results are well described by:

$$\log_{10}\langle N_{\text{WBH}} \rangle = A \log_{10}\left(\frac{M_{200}}{10^{12} M_\odot}\right) + B, \quad (1)$$

with $A = 1.17 \pm 0.17$ and $B = 0.95 \pm 0.22$ ³. The quasi-linear nature of the $\langle N_{\text{WBH}} \rangle - M_{200}$ relation is a key ingredient of this result. While the absolute normalization of the relation depends on the specific black hole seeding prescription adopted in **ROMULUS**, its slope is expected to be a robust feature of hierarchical structure formation. In particular, the accumulation of wandering black holes is driven primarily by the merger and accretion history of the host halo, rather than by the details of early black hole formation physics. Alternative seeding models may therefore shift the overall normalization of $\langle N_{\text{WBH}} \rangle$ (e.g., Untzaga et al. 2024), but are not expected to qualitatively alter the strong, monotonic increase of WBH abundance with halo mass.

To express this relation in terms of galaxy stellar mass, we adopt the stellar-to-halo mass relation (SHMR) parameterization of Moster et al. (2013),

$$M_*(M_{200}) = 2 N M_{200} \left[\left(\frac{M_{200}}{M_1}\right)^{-\beta} + \left(\frac{M_{200}}{M_1}\right)^\gamma \right]^{-1}, \quad (2)$$

with best-fit parameters at $z \simeq 0$ of $\log_{10}(M_1/M_\odot) = 11.6 \pm 0.2$, $N = 0.035 \pm 0.010$, $\beta = 1.38 \pm 0.15$, and

³ Only the average number of WBHs per bin (of 0.5 dex in halo mass) is given by Ricarte et al. (2021b), such that our uncertainties are based only on the scatter introduced by the somewhat large bin size.

$\gamma = 0.61 \pm 0.06$. This mapping is shown in the middle left panel of Fig. 2.

Finally, to account for the abundance of galaxies as a function of stellar mass, we adopt the local galaxy stellar mass function (GSMF) of Baldry et al. (2012), parameterized as a double Schechter function,

$$\phi_{\text{gal}}(M_{\star}) dM_{\star} = \ln(10) e^{-M_{\star}/M^*} \times \left[\phi_1^* \left(\frac{M_{\star}}{M^*} \right)^{\alpha_1+1} + \phi_2^* \left(\frac{M_{\star}}{M^*} \right)^{\alpha_2+1} \right] d \log_{10} M_{\star}, \quad (3)$$

with parameters $\log_{10}(M^*/M_{\odot}) = 10.66 \pm 0.02$, $\phi_1^* = (3.96 \pm 0.34) \times 10^{-3} \text{ Mpc}^{-3}$, $\alpha_1 = -0.35 \pm 0.10$, $\phi_2^* = (0.79 \pm 0.07) \times 10^{-3} \text{ Mpc}^{-3}$, and $\alpha_2 = -1.47 \pm 0.05$. The GSMF is shown in middle right panel of Fig. 2.

The volumetric density of wandering black holes as a function of parent galaxy stellar mass is then given by

$$\phi_{\text{WBH}}(M_{\star}) \propto \phi_{\text{gal}}(M_{\star}) \langle N_{\text{WBH}}[M_{200}(M_{\star})] \rangle. \quad (4)$$

Equation (4) captures the competing effects that shape the WBH demographics. Low-mass galaxies ($\log_{10}(M_{\star}/M_{\odot}) \lesssim 10$) dominate the galaxy number density but host, on average, $\langle N_{\text{WBH}} \rangle \lesssim 1$ wandering black hole per system. Conversely, very massive galaxies ($\log_{10}(M_{\star}/M_{\odot}) \gtrsim 11.3$) host many hundreds to thousands of WBHs each, but are exponentially rare. As a result, their product peaks at intermediate-to-high stellar masses, where galaxies are both sufficiently common and individually rich in wandering black holes.

The resulting $\phi_{\text{WBH}}(M_{\star})$ is shown by the purple curve in Fig. 3. The distribution peaks sharply at $\log_{10}(M_{\star}/M_{\odot}) = 11.10^{+0.05}_{-0.10}$ (note the log scale). The cumulative distribution, shown in yellow, indicates that more than 50% of all wandering black holes in the local Universe reside in galaxies with $10.7 \lesssim \log_{10}(M_{\star}/M_{\odot}) \lesssim 11.2$. All currently known off-nuclear TDE parent galaxies fall squarely within this dominant interval (Table 1).

The observed preference of off-nuclear TDEs for massive, early-type galaxies therefore follows naturally from the demographics of wandering black holes. Even with the probability for an individual WBH to produce a TDE been independent of parent galaxy properties, the observed parent-galaxy distribution will cluster around $M_{\star} \sim 10^{11} M_{\odot}$, simply because this is where the cosmic density of wandering black holes is maximized. In this sense, the parent-galaxy preference of off-nuclear TDEs is a purely demographic consequence of hierarchical structure formation.

Finally, the early-type morphology of the observed hosts is also consistent with this picture. In the mass range $10.7 \lesssim \log_{10}(M_{\star}/M_{\odot}) \lesssim 11.2$, the local galaxy population is dominated by quenched spheroids, while

star-forming late-type galaxies are already exponentially suppressed, as shown in the right panel of Fig. 2, which show the local GSMF divided in blue (star-forming) and red (quenched) galaxies. More specifically, in this mass range, red (quenched) galaxies are ~ 7 times more common than blue (star-forming) galaxies. The observed morphological preference therefore also follows from the same demographic peak in $\phi_{\text{WBH}}(M_{\star})$.

A clear prediction of this framework is that, as the sample of off-nuclear TDEs grows, their parent galaxies will continue to be drawn predominantly from the narrow stellar-mass range $10.7 \lesssim \log_{10}(M_{\star}/M_{\odot}) \lesssim 11.2$.

3.2. Stellar Counterparts

In addition to the preference for massive parent galaxies, the current sample of off-nuclear TDEs exhibits a apparent dichotomy in the detection of local stellar counterparts. Two events, 3XMM J2150–05 and EP240222a, are associated with clear stellar overdensities consistent with bound dwarf satellite galaxies, while AT2024tvd and AT2025abcr, show no detected stellar counterpart above the ambient halo background. This dichotomy is quantified by the stellar surface density contrast at the TDE position, $\Sigma_{\star,\text{local}}/\Sigma_{\star,\text{halo}}$, measured from deep pre-TDE imaging (in Appendix C) and reported in the final column of Table 1.

Both 3XMM J2150–05 and EP240222a, showing $\Sigma_{\star,\text{local}}/\Sigma_{\star,\text{halo}} > 3$, quantifying the fact the WBH remains embedded in a detectable stellar system. In contrast, both AT2024tvd and AT2025abcr have no detected overdensity and therefore (by definition) $\Sigma_{\star,\text{local}}/\Sigma_{\star,\text{halo}} \equiv 1$.

Figure 4 places the observed off-nuclear TDEs in the context of the stellar overdensity properties of WBHs predicted by ROMULUS. The background points show the simulated population at $z \simeq 0.05$, color-coded by halo-centric distance R_{\bullet}/R_{200} , while the stars mark the locations of the four observed events. In ROMULUS, the stellar overdensity associated with each wandering black hole is defined as the ratio of the stellar mass enclosed within a fixed physical aperture of 1 kpc centered on the black hole to the mean stellar density of the host halo at the same halo-centric radius, $\rho_{\star,\text{local}}/\rho_{\star,\text{halo}}$ (Ricarte et al. 2021b). This metric quantifies whether a wandering black hole remains embedded in a bound stellar system or has been effectively stripped of its extended stellar envelope.

Our observational measurements necessarily rely on projected quantities. We therefore characterize the stellar environments of the observed off-nuclear TDEs using the analogous surface-density ratio $\Sigma_{\star,\text{local}}/\Sigma_{\star,\text{halo}}$. While this differs formally from the three-dimensional

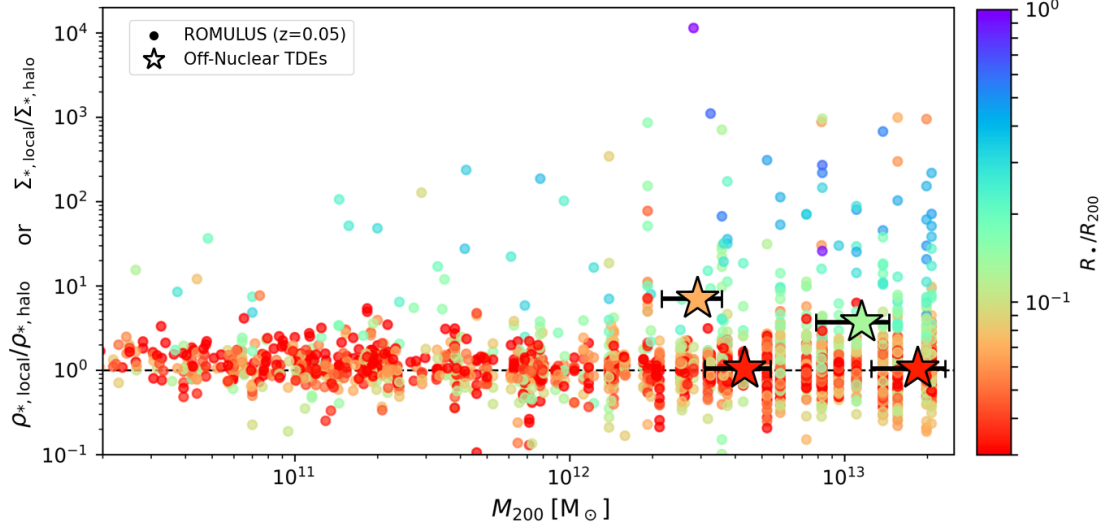


Figure 4. Stellar overdensity around wandering black holes as a function of host halo mass. Colored circles show the ROMULUS (Ricarte et al. 2021b) wandering black hole population at $z \simeq 0.05$, with color indicating halo-centric radius R_\bullet/R_{200} . The vertical axis gives the stellar overdensity around the WBHs, $\rho_{*,\text{local}}/\rho_{*,\text{halo}}$. Stars denote observed off-nuclear TDEs, for which the analogous projected quantity $\Sigma_{*,\text{local}}/\Sigma_{*,\text{halo}}$ is measured. Events associated with surviving dwarf satellites (3XMM J2150–05 and EP240222a) populate the high-overdensity tail, while events without detected stellar counterparts (AT2024tvd and AT2025abcr) fall within the dominant population of stripped WBHs. The bimodality between stellar overdensity and halo-centric radius seen in the simulation is also reflected in the current off-nuclear TDE sample.

definition used in the simulation, both quantities scale monotonically with enclosed stellar mass for compact systems, providing a directly comparable classification of stellar-embedded versus stripped objects.

A central point illustrated by Fig. 4 is that the physically relevant quantity governing the stellar environment of a wandering black hole is the normalized halo-centric distance, R_{TDE}/R_{200} , rather than the projected offset on the sky, $R_{\text{TDE},p}$, even if in physical (kpc) scale. This dimensionless radius scale with strength of the tidal field experienced by the system and therefore controls the efficiency of stellar stripping; it is encoded by the color scale in the figure. In massive halos, a large projected separation from the galaxy nucleus does not necessarily imply a large normalized halo-centric distance.

This is clearly illustrated by comparing 3XMM J2150–05 and AT2025abcr using the values in Table 1. Despite having comparable projected offsets ($R_{\text{TDE},p} \simeq 10$ kpc), the two events occupy different positions within their host halos (e.g., see their different colors in Fig. 4). 3XMM J2150–05 lies at $R_{\text{TDE}}/R_{200} \simeq 0.05$, while AT2025abcr, hosted by a more massive halo with a larger virial radius (see Table 1), resides deeper in the potential at $R_{\text{TDE}}/R_{200} \simeq 0.02$. This places the two systems in qualitatively different tidal regimes, naturally explaining why the former retains a dense stellar counterpart while the latter does not. In this sense, $R_{\text{TDE},p}$ alone can be misleading, as

it does not capture the depth of the system within the host halo.

Importantly, a stellar overdensity ratio consistent with unity does not imply that a wandering black hole is entirely devoid of orbiting stars. Both the simulation and the observations probe stellar structure on 100’s pc scales, limited by stellar particle mass resolution in ROMULUS and by surface-brightness sensitivity and PSF smearing in the imaging data. Compact stellar systems—such as dense nuclear star clusters originally associated with the black hole—are more resilient to tidal stripping (Van Wassenhove et al. 2014; Tremmel et al. 2018b), yet may remain unresolved or undetectable at the available resolution. Such components could nonetheless be sufficiently massive and dense to sustain a detectable TDE rate, even in the absence of an extended/detectable stellar counterpart.

As the observed sample grows, we therefore expect the fraction of events with detectable stellar counterparts to remain (in general terms) a bimodal function of halo-centric radius. Finally, we note that an additional population of off-nuclear black holes may reside in even more compact stellar systems, such as globular clusters. While no TDE has yet been securely identified in a globular cluster, dynamical evidence suggests that some massive clusters (e.g., ω Centauri in the Milky Way, Haberle et al. 2024) likely host IMBHs. Such systems would fall below the resolution and surface-brightness limits of both current cosmological simulations and most

extragalactic imaging, yet could in principle contribute to the off-nuclear TDE population.

3.3. Radial Distribution

The final demographic property of the current off-nuclear TDE sample is the wide range of halo-centric radii at which these events occur. From the deprojected offsets listed in Table 1, the four events span nearly two orders of magnitude in normalized radius, from $R_{\text{TDE}}/R_{200} \simeq 0.003$ (AT2024tvd) to $R_{\text{TDE}}/R_{200} \simeq 0.11$ (EP240222a).

Figure 5 compares these locations to the radial distribution of wandering black holes predicted by ROMULUS. The blue and teal curves show the simulated halo-centric distributions, $dN/d(R_{\bullet}/R_{200})$, at $z = 0.05$ for halos with $\log_{10}(M_{200}/M_{\odot}) = 12.5\text{--}13$ and $13\text{--}13.5$, respectively, while the red kernels mark the observed events. In the simulations, most wandering black holes reside at $0.01 \lesssim R_{\bullet}/R_{200} \lesssim 0.1$, with a declining tail toward both smaller and larger radii.

The observed off-nuclear TDEs fall within this predicted range. AT2024tvd, at $R_{\text{TDE}}/R_{200} \simeq 0.003$, lies near the inner edge of the simulated distribution, where wandering black holes are rare and typically in the final stages of orbital decay toward the halo center. Accordingly, the discovery of additional off-nuclear TDEs at similarly small halo-centric radii to AT2024tvd is expected to be rare. The remaining events sample the main body and outer tail of the distribution.

Overall, the radial locations of the current off-nuclear TDE sample are fully consistent with the expectations for wandering black holes in massive halos.

4. CONCLUSION

The growing sample of secure off-nuclear TDEs provides direct empirical evidence for, and a path to the study of the long-predicted population of off-nuclear massive black holes ($M_{\bullet} \geq 10^4 M_{\odot}$). Despite the small sample size, these events already exhibit two demographic patterns: (i) all occur in massive, early-type galaxies with $M_{\star} \simeq 10^{11} M_{\odot}$; and (ii) events at larger halo-centric radii are associated with detectable satellite dwarfs, whereas those deeper in their parent galaxy halo lack stellar counterpart.

In this *Letter* we showed that both trends can be extracted from the ROMULUS simulations and are therefore general expectations of hierarchical galaxy assembly. By combining the simulation’s WBH occupation statistics with empirical constraints on the local galaxy population, we computed the volumetric WBH density as a function of parent stellar mass, $\phi_{\text{WBH}}(M_{\star})$. This distribution peaks sharply at $M_{\star} = 10^{11} M_{\odot}$ and places the

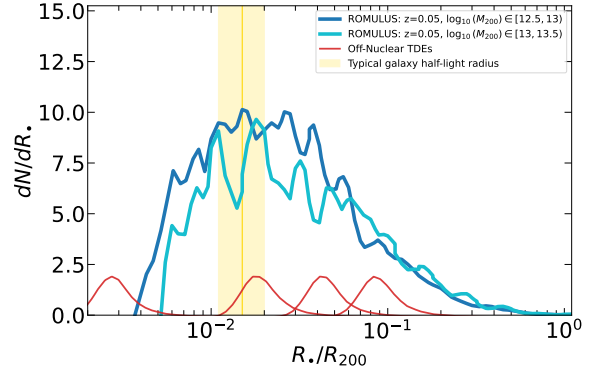


Figure 5. Radial distribution of wandering black holes in ROMULUS compared to the observed locations of off-nuclear TDEs. Blue and teal curves show the halo-centric distributions, $dN/d(R_{\bullet}/R_{200})$, of wandering black holes at $z = 0.05$ for halos with $\log_{10}(M_{200}/M_{\odot}) = 12.5\text{--}13$ and $13\text{--}13.5$, respectively (Ricarte et al. 2021b). Red kernels mark the deprojected halo-centric radii of the four observed off-nuclear TDEs. Yellow line and contour illustrate the typical half-light radius ($R_{1/2}$) of galaxies.

majority of WBHs in the local Universe in parent galaxies within the narrow range $10.7 \lesssim \log_{10}(M_{\star}/M_{\odot}) \lesssim 11.2$, naturally explaining why the entire off-nuclear TDE sample is located in galaxies with such mass range.

We further showed that the observed presence or absence of a detectable stellar counterpart follows from tidal stripping. In ROMULUS, WBHs that retain resolved stellar overdensities (e.g., bound dwarf satellites, as observed for 3XMM J215-05 and EP20240222a) preferentially reside at larger halo-centric radii, while the dominant population at smaller R_{\bullet}/R_{200} has overdensities near unity, consistent with the non-detection of stellar counterpart for AT2024tvd and AT2025abcr.

Taken together, these results support a simple interpretation: off-nuclear TDEs are transient accretion signposts of the WBH population long predicted by cosmological simulations. As the sample expands with wide-field time-domain surveys, two clear, testable predictions follow: parent galaxies should continue to cluster around $10.7 \lesssim \log_{10}(M_{\star}/M_{\odot}) \lesssim 11.2$, and the bimodality in the relation between stellar overdensity and halo-centric radius should, with a few exceptions, persist. The growing sample of off-nuclear TDEs will therefore provide increasingly stringent tests of off-nuclear massive black hole demographics, satellite disruption, and hierarchical structure formation.

Acknowledgments – MG is grateful to Suvi Gezari and Andrew Mummery for their comments on an early version of this paper, and to Angelo Ricarte for a valuable discussion on wandering black holes.

APPENDIX

A. FROM M_* AND $R_{1/2}$ TO M_{200} AND R_{200}

We estimate the virial mass (M_{200}) and corresponding virial radius (R_{200}) of each galaxy from its stellar mass (M_*), projected half-light radius ($R_{1/2}$), and redshift (z) using a Bayesian framework that combines the stellar-to-halo mass relation (SHMR) with the empirical size–halo relation. The SHMR provides a monotonic mapping between stellar and halo mass, reflecting the efficiency of baryon conversion into stars across cosmic time. We adopt the functional form of [Moster et al. \(2013\)](#), as shown in Equation 2, with an intrinsic scatter of $\sigma_{\log M_*} = 0.1$ dex.

Galaxy size information is incorporated through the empirical scaling between the half-light radius and halo radius, $R_{1/2} = f_{\text{size}} R_{200}$, which encapsulates the structural coupling between galaxies and their host halos.

For early-type (quenched) systems, we adopt a prior $f_{\text{size}} = 0.015$ with a lognormal dispersion $\sigma_{\log f} = 0.1$ dex, consistent with observed size–halo relations for massive ellipticals (e.g., [Kravtsov 2013](#)). Both M_{200} and f_{size} are treated as free parameters, and their joint posterior distribution is sampled using `emcee` ([Foreman-Mackey et al. 2013](#)).

The likelihood simultaneously constrains the stellar and structural observables as

$$\ln \mathcal{L} = -\frac{1}{2} \left[\frac{(\log M_*^{\text{obs}} - \log M_*^{\text{model}}(M_{200}))^2}{\sigma_{\log M_*}^2} \right] + \frac{1}{2} \left[\frac{(\log R_{1/2}^{\text{obs}} - \log(f_{\text{size}} R_{200}(M_{200})))^2}{\sigma_{\log R}^2} \right], \quad (\text{A1})$$

where $\sigma_{\log R} = 0.1$ dex represents the intrinsic scatter in the size–halo relation.

For each MCMC sample, the virial radius is computed from the corresponding halo mass using

$$M_{200} = \frac{4}{3} \pi R_{200}^3 \rho_c(z), \quad (\text{A2})$$

where $\rho_c(z)$ is the critical density of the Universe at redshift z . The critical density evolves with redshift as $\rho_c(z) = \frac{3H^2(z)}{8\pi G}$, where G is the gravitational constant and $H(z)$ is the Hubble parameter at redshift z . The latter is obtained from the cosmological expansion law in a flat Λ CDM model, $H(z) = H_0 \sqrt{\Omega_m(1+z)^3 + \Omega_\Lambda}$, so that $\rho_c(z)$ increases with redshift. This evolving critical density defines the overdensity threshold used to calculate virial masses and radii.

Overall, this approach combines stellar mass and galaxy size information to infer self-consistent halo prop-

erties while naturally incorporating observational scatter and empirical scaling uncertainties.

B. GALAXY MASSES

We estimate parent-galaxy stellar masses in a homogeneous manner using optical photometry from the Legacy Survey Data Release 10 ([Dey et al. 2019](#)), following the color–dependent mass-to-light ratio prescription of [Baldry et al. \(2012\)](#). Total galaxy fluxes are measured from the best-fitting TRACTOR Sérsic models in the g and i bands.

All photometry is corrected for Galactic extinction using the dust maps of [Schlafly & Finkbeiner \(2011\)](#) and the extinction law of [Cardelli et al. \(1989\)](#). Stellar masses are then computed from the extinction-corrected i -band luminosity and the rest-frame color ($g - i)_0$ via

$$\log_{10}(M_*/L_i) = a + b(g - i)_0, \quad (\text{B3})$$

with coefficients $a = -0.68 \pm 0.05$ and $b = 0.73 \pm 0.05$, as calibrated by [Baldry et al. \(2012\)](#). Luminosity distances are calculated assuming a flat Λ CDM cosmology with $H_0 = 69 \text{ km s}^{-1} \text{ Mpc}^{-1}$.

Uncertainties on M_* include contributions from photometric errors in the g and i band and the intrinsic scatter in the mass-to-light ratio calibration. We assume no internal extinction within the parent galaxies, which is a reasonable approximation for quenched systems.

By using Sérsic luminosities, as in [Baldry et al. \(2012\)](#), we ensure that the effective aperture is not fixed but instead scales with galaxy distance and physical size. This guarantees that stellar masses are measured consistently across the sample and can be meaningfully compared. Importantly, by adopting the exact same methodology as [Baldry et al. \(2012\)](#), we ensure that our inferred stellar masses are directly comparable to those entering the galaxy stellar mass function used throughout this work.

C. COMPUTING $\Sigma_{*,\text{LOCAL}}/\Sigma_{*,\text{HALO}}$ FOR 3XMM J2150–05 AND EP240222A

To characterize the local stellar environments of the two off-nuclear TDE associated with dwarf satellites, EP240222a and 3XMM J2150–05, we compute the ratio between the local and ambient stellar surface densities, $\Sigma_{*,\text{local}}/\Sigma_{*,\text{halo}}$, using deep optical pre-TDE imaging. For 3XMM J2150–05 we use a 1999 *HST*/WFPC2 image on filter F814W, while for EP240222a use use Legacy Survey r –band image from 2014. This quantity provides a projected, observational analogue to the lo-

cal stellar density contrast used in numerical studies of wandering black holes (e.g., [Ricarte et al. 2021b](#)).

For each system, we define a narrow slit connecting the host galaxy nucleus and the transient position, along which a one-dimensional flux profile is measured. The slit defines the radial direction of the galaxy in projection and serves to locate the transient relative to the host and to visualize the local environment (upper right panel in Fig. 6).

The local stellar surface density, $\Sigma_{*,\text{local}}$, is measured within a circular aperture (red in Fig. 6) with a radius that is $3\times$ the image Point Spread Function (PSF), $\sim 0.15''$ *HST*/WFPC2 and $\sim 1''$ for Legacy, centered on the dwarf position. The ambient halo surface density, $\Sigma_{*,\text{halo}}$, is estimated using two rectangular regions placed perpendicular to the slit direction at the same projected host-centric radius as the dwarf (yellow in Fig. 6). These regions sample the surrounding stellar light while excluding the dwarf. Both $\Sigma_{*,\text{local}}$ and $\Sigma_{*,\text{halo}}$ are computed as the mean surface brightness within their respective regions, minimizing sensitivity to outliers and small-scale substructure.

We convert the measured surface brightness ratio into a stellar surface-density ratio by assuming that the stellar mass-to-light ratio is the same in the local and halo regions. This assumption is reasonable for these systems, as the off-nuclear transients are associated with compact dwarf hosts that exhibit old stellar populations ([Lin et al. 2018](#); [Jin et al. 2025](#)). The ratio $\Sigma_{*,\text{local}}/\Sigma_{*,\text{halo}}$ is then computed directly from the median surface densities.

For AT2024tvd and AT2025abcr, no statistically significant local overdensity is detected ([Yao et al. 2025](#); [Stein et al. 2026](#)); for these systems we therefore set $\Sigma_{*,\text{local}}/\Sigma_{*,\text{halo}} = 1$ by definition.

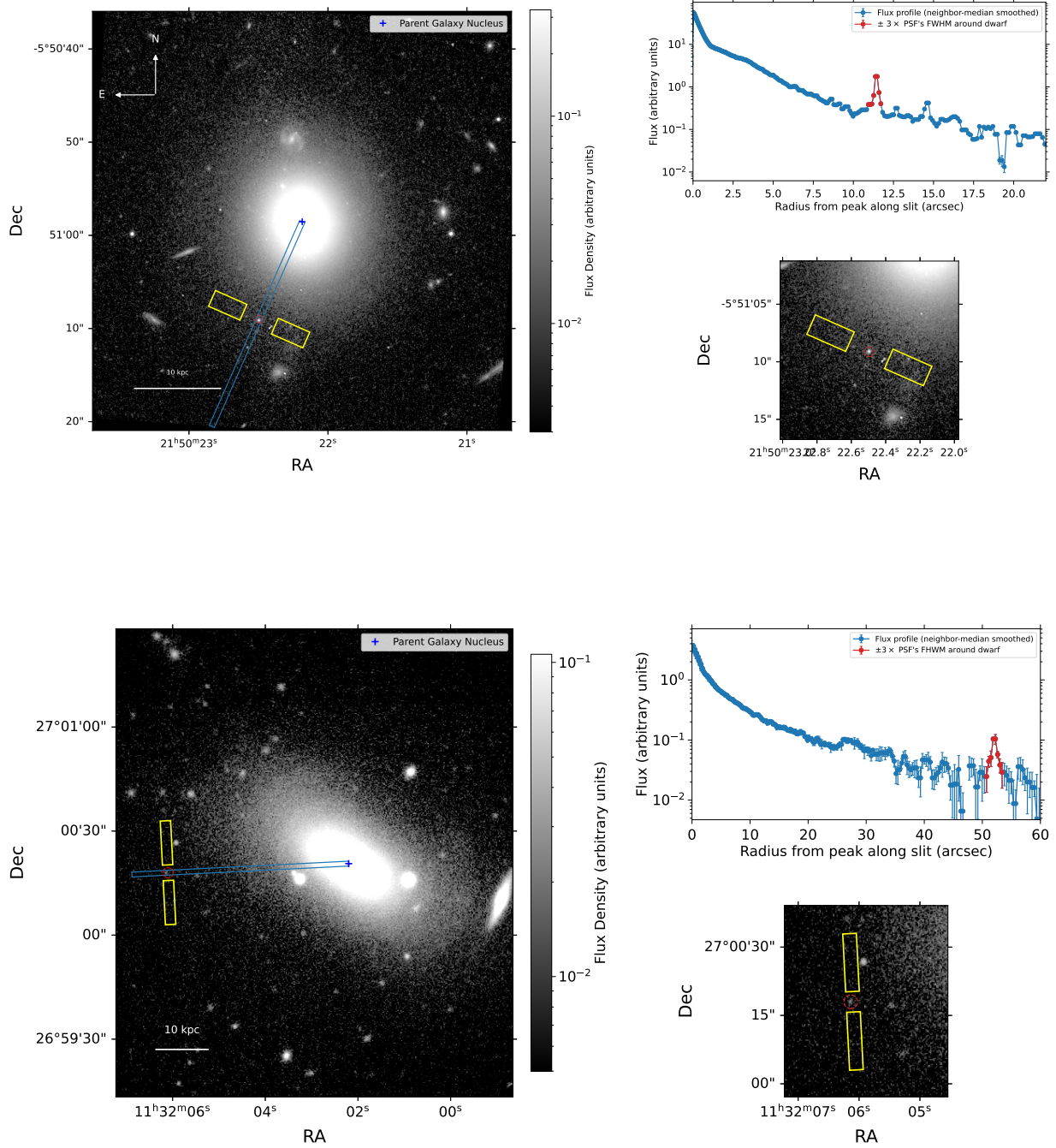


Figure 6. Stellar counterparts of the off-nuclear TDEs 3XMM J2150-05 (Top) and EP240222a (Bottom). For each system, the left panel shows the parent galaxy image (pre-TDE) with the slit connecting the galaxy nucleus to the dwarf galaxy position (blue) and the two rectangular regions used to estimate the ambient halo surface density (yellow), placed perpendicular to the slit at the same projected host-centric radius. The right panel shows the radial flux profile measured along the slit, with red points highlighting the region around the dwarf galaxy location. The lower panels show zoomed views of the dwarf environments, including the local aperture (red) and the halo comparison regions (yellow). These regions are used to compute the ratio $\Sigma_{*,\text{local}}/\Sigma_{*,\text{halo}}$ shown in Table 1.

REFERENCES

Amaro-Seoane, P., Audley, H., Babak, S., et al. 2017, arXiv e-prints, arXiv:1702.00786, doi: [10.48550/arXiv.1702.00786](https://doi.org/10.48550/arXiv.1702.00786)

Baldry, I. K., Driver, S. P., Loveday, J., et al. 2012, MNRAS, 421, 621, doi: [10.1111/j.1365-2966.2012.20340.x](https://doi.org/10.1111/j.1365-2966.2012.20340.x)

Begelman, M. C., Blandford, R. D., & Rees, M. J. 1980, Nature, 287, 307, doi: [10.1038/287307a0](https://doi.org/10.1038/287307a0)

Bellm, E. C., Kulkarni, S. R., Graham, M. J., et al. 2019, PASP, 131, 018002, doi: [10.1088/1538-3873/aaecbe](https://doi.org/10.1088/1538-3873/aaecbe)

Bellovary, J. M., Governato, F., Quinn, T. R., et al. 2010, ApJL, 721, L148, doi: [10.1088/2041-8205/721/2/L148](https://doi.org/10.1088/2041-8205/721/2/L148)

Cardelli, J. A., Clayton, G. C., & Mathis, J. S. 1989, ApJ, 345, 245, doi: [10.1086/167900](https://doi.org/10.1086/167900)

Chandrasekhar, S. 1943, ApJ, 97, 255, doi: [10.1086/144517](https://doi.org/10.1086/144517)

Chang, Y.-C., Soria, R., Kong, A. K. H., et al. 2025, ApJ, 983, 109, doi: [10.3847/1538-4357/adbbee](https://doi.org/10.3847/1538-4357/adbbee)

Charalampopoulos, P., Leloudas, G., Malesani, D. B., et al. 2022, A&A, 659, A34, doi: [10.1051/0004-6361/202142122](https://doi.org/10.1051/0004-6361/202142122)

Colpi, M. 2014, SSRv, 183, 189, doi: [10.1007/s11214-014-0067-1](https://doi.org/10.1007/s11214-014-0067-1)

Comerford, J. M., & Greene, J. E. 2014, ApJ, 789, 112, doi: [10.1088/0004-637X/789/2/112](https://doi.org/10.1088/0004-637X/789/2/112)

Comerford, J. M., Griffith, R. L., Gerke, B. F., et al. 2009, ApJL, 702, L82, doi: [10.1088/0004-637X/702/1/L82](https://doi.org/10.1088/0004-637X/702/1/L82)

Dey, A., Schlegel, D. J., Lang, D., et al. 2019, AJ, 157, 168, doi: [10.3847/1538-3881/ab089d](https://doi.org/10.3847/1538-3881/ab089d)

Donato, D., Cenko, S. B., Covino, S., et al. 2014, ApJ, 781, 59, doi: [10.1088/0004-637X/781/2/59](https://doi.org/10.1088/0004-637X/781/2/59)

Farrell, S. A., Webb, N. A., Barret, D., Godet, O., & Rodrigues, J. M. 2009, Nature, 460, 73, doi: [10.1038/nature08083](https://doi.org/10.1038/nature08083)

Ferrarese, L., & Merritt, D. 2000, ApJL, 539, L9, doi: [10.1086/312838](https://doi.org/10.1086/312838)

Foreman-Mackey, D., Hogg, D. W., Lang, D., & Goodman, J. 2013, PASP, 125, 306, doi: [10.1086/670067](https://doi.org/10.1086/670067)

Gezari, S., Hammerstein, E., Yao, Y., et al. 2021, Transient Name Server AstroNote, 103, 1

Governato, F., Colpi, M., & Maraschi, L. 1994, MNRAS, 271, 317, doi: [10.1093/mnras/271.2.317](https://doi.org/10.1093/mnras/271.2.317)

Grotova, I., Rau, A., Baldini, P., et al. 2025, A&A, 697, A159, doi: [10.1051/0004-6361/202553669](https://doi.org/10.1051/0004-6361/202553669)

Gültekin, K., Richstone, D. O., Gebhardt, K., et al. 2009, ApJ, 698, 198, doi: [10.1088/0004-637X/698/1/198](https://doi.org/10.1088/0004-637X/698/1/198)

Guolo, M., Gezari, S., Yao, Y., et al. 2024, ApJ, 966, 160, doi: [10.3847/1538-4357/ad2f9f](https://doi.org/10.3847/1538-4357/ad2f9f)

Guolo, M., & Mummery, A. 2025, ApJ, 978, 167, doi: [10.3847/1538-4357/ad990a](https://doi.org/10.3847/1538-4357/ad990a)

Guolo, M., Mummery, A., van Velzen, S., et al. 2025, arXiv e-prints, arXiv:2510.26774, doi: [10.48550/arXiv.2510.26774](https://doi.org/10.48550/arXiv.2510.26774)

—. 2026, arXiv e-prints, arXiv:2602.12272, <https://arxiv.org/abs/2602.12272>

Gwyn, S. D. J. 2012, AJ, 143, 38, doi: [10.1088/0004-6256/143/2/38](https://doi.org/10.1088/0004-6256/143/2/38)

Haberle, M., Neumayer, N., Seth, A., et al. 2024, Nature, 631, 285, doi: [10.1038/s41586-024-07511-z](https://doi.org/10.1038/s41586-024-07511-z)

Hammerstein, E., Gezari, S., van Velzen, S., et al. 2021, ApJL, 908, L20, doi: [10.3847/2041-8213/abdc4](https://doi.org/10.3847/2041-8213/abdc4)

Ho, A. Y. Q., Perley, D. A., Gal-Yam, A., et al. 2023, ApJ, 949, 120, doi: [10.3847/1538-4357/acc533](https://doi.org/10.3847/1538-4357/acc533)

Islam, R. R., Taylor, J. E., & Silk, J. 2004, MNRAS, 354, 427, doi: [10.1111/j.1365-2966.2004.08201.x](https://doi.org/10.1111/j.1365-2966.2004.08201.x)

Jin, C. C., Li, D. Y., Jiang, N., et al. 2025, arXiv e-prints, arXiv:2501.09580, doi: [10.48550/arXiv.2501.09580](https://doi.org/10.48550/arXiv.2501.09580)

Kaaret, P., Feng, H., & Roberts, T. P. 2017, ARA&A, 55, 303, doi: [10.1146/annurev-astro-091916-055259](https://doi.org/10.1146/annurev-astro-091916-055259)

Knollmann, S. R., & Knebe, A. 2009, ApJS, 182, 608, doi: [10.1088/0067-0049/182/2/608](https://doi.org/10.1088/0067-0049/182/2/608)

Kormendy, J., & Ho, L. C. 2013, ARA&A, 51, 511, doi: [10.1146/annurev-astro-082708-101811](https://doi.org/10.1146/annurev-astro-082708-101811)

Kravtsov, A. V. 2013, ApJL, 764, L31, doi: [10.1088/2041-8205/764/2/L31](https://doi.org/10.1088/2041-8205/764/2/L31)

Lin, D., Strader, J., Carrasco, E. R., et al. 2018, Nature Astronomy, 2, 656, doi: [10.1038/s41550-018-0493-1](https://doi.org/10.1038/s41550-018-0493-1)

Lin, D., Strader, J., Romanowsky, A. J., et al. 2020, ApJL, 892, L25, doi: [10.3847/2041-8213/ab745b](https://doi.org/10.3847/2041-8213/ab745b)

Magorrian, J., Tremaine, S., Richstone, D., et al. 1998, AJ, 115, 2285, doi: [10.1086/300353](https://doi.org/10.1086/300353)

Maksym, W. P., Ulmer, M. P., Eracleous, M. C., Guennou, L., & Ho, L. C. 2013, MNRAS, 435, 1904, doi: [10.1093/mnras/stt1379](https://doi.org/10.1093/mnras/stt1379)

Maksym, W. P., Ulmer, M. P., Roth, K. C., et al. 2014, MNRAS, 444, 866, doi: [10.1093/mnras/stu1485](https://doi.org/10.1093/mnras/stu1485)

Menon, H., Wesolowski, L., Zheng, G., et al. 2015, Computational Astrophysics and Cosmology, 2, 1, doi: [10.1186/s40668-015-0007-9](https://doi.org/10.1186/s40668-015-0007-9)

Moster, B. P., Naab, T., & White, S. D. M. 2013, MNRAS, 428, 3121, doi: [10.1093/mnras/sts261](https://doi.org/10.1093/mnras/sts261)

Mummery, A., & van Velzen, S. 2025, arXiv e-prints, arXiv:2410.17087, doi: [10.48550/arXiv.2410.17087](https://doi.org/10.48550/arXiv.2410.17087)

Mummery, A., van Velzen, S., Nathan, E., et al. 2024, MNRAS, 527, 2452, doi: [10.1093/mnras/stad3001](https://doi.org/10.1093/mnras/stad3001)

Natarajan, P. 2014, General Relativity and Gravitation, 46, 1702, doi: [10.1007/s10714-014-1702-6](https://doi.org/10.1007/s10714-014-1702-6)

Ni, Y., Di Matteo, T., Bird, S., et al. 2022, MNRAS, 513, 670, doi: [10.1093/mnras/stac351](https://doi.org/10.1093/mnras/stac351)

Perley, D. A., Mazzali, P. A., Yan, L., et al. 2019, MNRAS, 484, 1031, doi: [10.1093/mnras/sty3420](https://doi.org/10.1093/mnras/sty3420)

Pfeffer, J., Griffen, B. F., Baumgardt, H., & Hilker, M. 2014, MNRAS, 444, 3670, doi: [10.1093/mnras/stu1705](https://doi.org/10.1093/mnras/stu1705)

Planck Collaboration, Aghanim, N., Akrami, Y., et al. 2020, A&A, 641, A6, doi: [10.1051/0004-6361/201833910](https://doi.org/10.1051/0004-6361/201833910)

Rees, M. J. 1988, Nature, 333, 523, doi: [10.1038/333523a0](https://doi.org/10.1038/333523a0)

Reines, A. E., Condon, J. J., Darling, J., & Greene, J. E. 2020, ApJ, 888, 36, doi: [10.3847/1538-4357/ab4999](https://doi.org/10.3847/1538-4357/ab4999)

Ricarte, A., Tremmel, M., Natarajan, P., & Quinn, T. 2021a, ApJL, 916, L18, doi: [10.3847/2041-8213/ac1170](https://doi.org/10.3847/2041-8213/ac1170)

Ricarte, A., Tremmel, M., Natarajan, P., Zimmer, C., & Quinn, T. 2021b, MNRAS, 503, 6098, doi: [10.1093/mnras/stab866](https://doi.org/10.1093/mnras/stab866)

Schlafly, E. F., & Finkbeiner, D. P. 2011, ApJ, 737, 103, doi: [10.1088/0004-637X/737/2/103](https://doi.org/10.1088/0004-637X/737/2/103)

Seth, A. C., van den Bosch, R., Mieske, S., et al. 2014, Nature, 513, 398, doi: [10.1038/nature13762](https://doi.org/10.1038/nature13762)

Somalwar, J. J., Ravi, V., Margutti, R., et al. 2025, ApJ, 995, 228, doi: [10.3847/1538-4357/ae1501](https://doi.org/10.3847/1538-4357/ae1501)

Soria, R., Musaeva, A., Wu, K., et al. 2017, MNRAS, 469, 886, doi: [10.1093/mnras/stx888](https://doi.org/10.1093/mnras/stx888)

Stein, R., Carney, J., Ward, C., et al. 2026, arXiv e-prints, arXiv:2602.10180. <https://arxiv.org/abs/2602.10180>

Storchi-Bergmann, T., & Schnorr-Müller, A. 2019, Nature Astronomy, 3, 48, doi: [10.1038/s41550-018-0611-0](https://doi.org/10.1038/s41550-018-0611-0)

Sturm, M. R., Reines, A. E., Lohfink, A. M., et al. 2026, ApJ, 996, 41, doi: [10.3847/1538-4357/ae1eec](https://doi.org/10.3847/1538-4357/ae1eec)

Taylor, M. A., Tahmasebzadeh, B., Thompson, S., et al. 2025, ApJL, 991, L24, doi: [10.3847/2041-8213/ae028e](https://doi.org/10.3847/2041-8213/ae028e)

Tremaine, S., Gebhardt, K., Bender, R., et al. 2002, ApJ, 574, 740, doi: [10.1086/341002](https://doi.org/10.1086/341002)

Tremmel, M., Governato, F., Volonteri, M., Pontzen, A., & Quinn, T. R. 2018a, ApJL, 857, L22, doi: [10.3847/2041-8213/aabc0a](https://doi.org/10.3847/2041-8213/aabc0a)

Tremmel, M., Governato, F., Volonteri, M., & Quinn, T. R. 2015, MNRAS, 451, 1868, doi: [10.1093/mnras/stv1060](https://doi.org/10.1093/mnras/stv1060)

Tremmel, M., Governato, F., Volonteri, M., Quinn, T. R., & Pontzen, A. 2018b, MNRAS, 475, 4967, doi: [10.1093/mnras/sty139](https://doi.org/10.1093/mnras/sty139)

Tremmel, M., Karcher, M., Governato, F., et al. 2017, MNRAS, 470, 1121, doi: [10.1093/mnras/stx1160](https://doi.org/10.1093/mnras/stx1160)

Tremmel, M., Quinn, T. R., Ricarte, A., et al. 2019, MNRAS, 483, 3336, doi: [10.1093/mnras/sty3336](https://doi.org/10.1093/mnras/sty3336)

Untzaga, J., Bonoli, S., Izquierdo-Villalba, D., Mezcua, M., & Spinoso, D. 2024, MNRAS, 535, 3293, doi: [10.1093/mnras/stae2454](https://doi.org/10.1093/mnras/stae2454)

Uppal, A., Ward, C., Gezari, S., et al. 2024, ApJ, 975, 286, doi: [10.3847/1538-4357/ad7ff0](https://doi.org/10.3847/1538-4357/ad7ff0)

van Velzen, S., Gezari, S., Hammerstein, E., et al. 2021, ApJ, 908, 4, doi: [10.3847/1538-4357/abc258](https://doi.org/10.3847/1538-4357/abc258)

Van Wassenhove, S., Capelo, P. R., Volonteri, M., et al. 2014, MNRAS, 439, 474, doi: [10.1093/mnras/stu024](https://doi.org/10.1093/mnras/stu024)

Vogel, K. T., Seth, A. C., Baumgardt, H., et al. 2019, ApJ, 871, 159, doi: [10.3847/1538-4357/aaf735](https://doi.org/10.3847/1538-4357/aaf735)

Volonteri, M., Haardt, F., & Madau, P. 2003, ApJ, 582, 559, doi: [10.1086/344675](https://doi.org/10.1086/344675)

Wadsley, J. W., Keller, B. W., & Quinn, T. R. 2017, MNRAS, 471, 2357, doi: [10.1093/mnras/stx1643](https://doi.org/10.1093/mnras/stx1643)

Ward, C., Gezari, S., Frederick, S., et al. 2021, ApJ, 913, 102, doi: [10.3847/1538-4357/abf246](https://doi.org/10.3847/1538-4357/abf246)

Yao, Y., Ravi, V., Gezari, S., et al. 2023, ApJL, 955, L6, doi: [10.3847/2041-8213/acf216](https://doi.org/10.3847/2041-8213/acf216)

Yao, Y., Chornock, R., Ward, C., et al. 2025, ApJL, 985, L48, doi: [10.3847/2041-8213/add7de](https://doi.org/10.3847/2041-8213/add7de)

Yuan, W., Zhang, C., Ling, Z., et al. 2018, in Society of Photo-Optical Instrumentation Engineers (SPIE) Conference Series, Vol. 10699, Space Telescopes and Instrumentation 2018: Ultraviolet to Gamma Ray, ed. J.-W. A. den Herder, S. Nikzad, & K. Nakazawa, 1069925, doi: [10.1117/12.2313358](https://doi.org/10.1117/12.2313358)